Original article

Impact of micro-scale characteristics of shale reservoirs on gas depletion behavior: A microscale discrete model

Wangxing Cheng[1,2], Yingjie Guo[1,2], Guanglei Cui[1,2]⊙*, Derek Elsworth[3], Yuling Tan[4], Zhejun Pan[5]

[1]*Key Laboratory of Ministry of Education on Safe Mining of Deep Metal Mines, Northeastern University, Shenyang 110819, P. R. China*

[2]*Key Laboratory of Liaoning Province on Deep Engineering and Intelligent Technology, Northeastern University, Shenyang 110819, P. R. China*

[3]*Energy and Mineral Engineering, G3 Center and Energy Institute, Pennsylvania State University, University Park, PA 16802, USA*

[4]*Hebei Research Center of the Basic Discipline Engineering Mechanics, Shijiazhuang Tiedao University, Shijiazhuang 050043, P. R. China*

[5]*State Key Laboratory of Continental Shale Oil, Northeast Petroleum University, Daqing 163318, P. R. China*

Abstract:
Shale gas has become increasingly significant in the global energy supply. Mineral heterogeneity in shales importantly impacts gas transport within the shale matrix and therefore the depletion history curve. A microscale discrete coupling model is introduced to clarify mass transfer and mechanical interactions, as well as their impact on gas transport properties, ranging from individual mineral through ensemble field scale. The model uses a mineral morphology thin-section obtained through tescan integrated mineral analyzer with the mechanical parameters, controlling both elastic and viscosity behavior of each mineral, achieved through nanoindentation. A coupled model for poromechanical evolution is proposed and solved using COMSOL. The applicability of the model results are validated against field data using a dimensionless approach. This confirms that in the early stages of gas depletion, gas is primarily liberated from inorganic minerals, whereas in later stages, it is predominantly sourced from adsorbed gas from the organic matter. Over time, the permeability of the inorganic minerals decreases, and a higher Young's modulus of the minerals results in a greater ultimate permeability ratio. Evolution of the effective diffusion coefficient for the organic matter is controlled by multiple components. A negative correlation exists between mineral grain size and the creep effects, indicating that larger grain sizes result in smaller creep magnitudes during gas production. The Young's modulus of inorganic matter is inversely correlated with the diffusion coefficient, while an increase in the Young's modulus in the organic matter corresponds to a higher diffusion coefficient. The proposed model complements the traditional continuum dual-medium method and provides a clearer understanding of the interactions between minerals during gas depletion behavior.

1. Introduction

Among unconventional resources, shale gas is increasingly crucial in the current energy supply due to its vast reserves and rising production (Chen et al., 2015b; Feng et al., 2024). Unlike conventional reservoirs, shales have low permeability, consisting of fine grained organic matter, quartz, carbonates, pyrite, feldspar, and various clay minerals including illite and montmorillonite (Geng et al., 2016; Schwartz et al., 2019b; Wang et al., 2024a). Due to the substantial differences in the mechanical characteristics and flow properties of these

constituent minerals, there is evident coupling control between mass transfer and mechanics (Cui et al., 2018a, 2018b). Yet the impact of interactions among complex shale minerals on gas depletion characteristics at field scale has been largely overlooked (Monteiro et al., 2012; Cui et al., 2020b; Abdallah et al., 2023) despite, this knowledge being crucial in understanding production of gas from shales.

The mechanical properties and pore topology within shale matrix are highly heterogeneous (Li et al., 2009; Day-Stirrat et al., 2010; Abdallah et al., 2023). Atomic Force Microscopy and nanoindentation techniques are typically utilized to evaluate Young's modulus of different components in shale matrix at nanoscale (Eliyahu et al., 2015; Abedi et al., 2016). Atomic Force Microscopy facilitates three-dimensional mapping of surface roughness and modulus of different materials. Mapped surface morphology constrains the range of Young's modulus range for various minerals (Coq Germanicus et al., 2020; Liu et al., 2023b). Nanoindentation profiling, using the Oliver-Pharr model, can also provide ranges of Young's modulus for minerals (Oliver and Pharr, 1992). The Young's modulus of organic matter is typically < 25 GPa, whereas that of inorganic matter typically > 60 GPa (Cui et al., 2020b; Yang et al., 2020) . These observations suggest that heterogeneous mechanical properties may result in distinct mechanical behaviors in aggregates of inorganic and organic materials during gas depletion. Scanning electron microscopy (SEM) and transmission electron microscopy (TEM) are commonly employed to study the pore structure of the shale matrix (Javadpour et al., 2009; Loucks et al., 2009). two-dimensional images obtained through SEM imaging reveal finely dispersed porous organic matter (kerogen inclusions) embedded within the inorganic matrix (Ambrose et al., 2010; Tian et al., 2013; Yang et al., 2014). The inorganic matrix also contains pores and fractures of various sizes (Palmer and Mansoori, 1998; Chen et al., 2019; Tahmasebi et al., 2020). These complex and multiscale pore geometries are anticipated to result in significant structural differences in gas transport characteristics among different minerals and thus affecting mass transfer.

The variety of mineral species, contrasting mechanical properties and spectrum of pore types and distribution are all crucial factors influencing gas transport (Eliyahu et al., 2015; Li et al., 2019; Yang et al., 2020). Soft pores enclosed within a rigid matrix are known to exhibit different behavior compared to hard pores within a soft matrix (Schwartz et al., 2019b; Yang et al., 2020). Such heterogeneities result from the varied formation mechanisms of microscale pores and their interaction with the surrounding matrix. Hard and rigid minerals, such as quartz and calcite, typically form a dense structure, which restricts the permeability of liquids or gases (Tahmasebi et al., 2020). In contrast, soft phases, such as clay minerals, may develop larger numbers of pores or fractures (Jin et al., 2018; Yuan et al., 2018; Wang et al., 2022), thereby providing additional flow pathways and elevating permeability. Thus, clay content may play a crucial role in permeability evolution under stress (Al Ismail and Zoback, 2016). Permeability is typically positively correlated with quartz, feldspar and carbonate contents but negatively correlated with clay, pyrite, and total organic carbon (TOC) contents (Zhao et al., 2018). Mineral anisotropy also affects the evolution of permeability and furthermore gas depletion characteristics, with impacts remaining poorly resolved.

The impact of differences in Young's modulus of different minerals on permeability evolution has been broadly explored (Chen et al., 2015a; Geng et al., 2016; Zhang et al., 2018; Xie et al., 2022). The evolution of shale permeability at constant stress has been attributed it to the interaction between organic and inorganic matter (Shi et al., 2021). Coupled models have examinee permeability evolution during shale gas extraction suggesting that changes in shale permeability and gas production rates are largely controlled by the dynamic interface between mass and effective stress transfer between the matrix and fractures (Cui et al., 2018a). Nested microstructures have replicated the four-stage curve of permeability evolution including the impact of fractures (Peng et al., 2015; Liu et al., 2023a). At field scale, gas depletion curves show a precipitous decline to an asymptote sometimes interpreted as radial depletion reaching progressively farther with time and thus increasing effective diffusion lengths (Cui et al., 2020b). These approaches simplify reservoir microscopic properties to include only the effect of two microstructures: Matrix-fracture or organic-inorganic and neglect the severe complexity of the contribution of heterogeneity at microscale.

In summary, mineral interactions are vital factors affecting the evolution of permeability; however, existing permeability models often neglect the impact of this heterogeneity. This over-simplification is addressed through a geometric model that incorporates distributed mineral phases, capturing the mechanical and flow characteristics of individual minerals based on nanoindentation and Tescan Integrated Mineral Analyzer (TIMA) distribution testing and evaluations. A coupling model that accounts for the interaction between minerals is developed to examine the effect of various mineral phases on shale permeability and resulting gas production.

2. Mathematical model

This impact of heterogeneity is addressed through a series of partial differential equations that govern solid deformation and concurrent gas transport, utilizing a method akin to poroelastic theory. First, heterogeneity in the shale matrix is captured by explicitly separating organic and inorganic domains using TIMA-derived mineral maps. These maps provide spatially resolved porosity, permeability, and mechanical properties, ensuring that local variations in mineral composition and pore structure are accurately represented. Second, for the derivation and application of these equations, several fundamental assumptions are established: (a) The porous medium comprises two components: Solid and fluid; (b) the compressible rock pores and matrix skeleton conform to poroelastic theory; (c) the free gas in the pores is "ideal" with viscosity constant under isothermal conditions; (d) the rheology of the porous medium is represented by Burgers model; (e) the simulation is conducted under isothermal conditions; and (f) the gas is a single component with no competitive interactions. The model operates at the microscale for pore-level mechanics and transport and is validated against field-scale data through

dimensionless analysis.

2.1 Matrix deformatione

Based on the theory of poroelasticity, by drawing an analogy between thermal contraction and matrix contraction, the effects of pore pressure and adsorption stress may be accommodated. Creep is expressed in terms of strain and in accommodating creep compliance, the Navier-type constitutive deformation relationship is (Wang et al., 2024b):

$$Gu_{i,kk} + \frac{G}{1-2v}u_{k,ki} + \frac{\varepsilon_{c,i}}{L_{,i}} = f_i + \alpha_{in}p_{in,i} \tag{1}$$

$$Gu_{i,kk} + \frac{G}{1-2v}u_{k,ki} + \frac{\varepsilon_{c,i}}{L_{,i}} = f_i + \alpha_{or}p_{or,i} + K\varepsilon_{s,i}(p_{or}) \tag{2}$$

where u_i is the displacement in the i-direction, $u_{i,kk}$ is the second spatial derivative of the displacement component u_i, v is Poisson's ratio, u_k is the displacement in the k-direction, $u_{k,ki}$ divergence of the displacement vector, p is the gas pressure, $\varepsilon_{s,i}$ is the adsorption strain obtained from the Langmuir equation in the i-direction, $\varepsilon_{c,i}$ is the creep strain in the i-direction, α_{in} and α_{or} are the Biot coefficient, K is the bulk modulus and G is the shear modulus. Subscripts, in and or represent inorganic and organic systems, respectively and $L_{,i}$ represents the creep compliance in the i-direction. i and k represent the three directions of x, y, and z.

Shale microcreep mechanics readily conforms to the Burgers model. The constitutive relationship linking strain to stress is:

$$\varepsilon_c = \frac{\sigma_0}{E_1} + \frac{\sigma_0}{E_2}\left(1 - e^{-\frac{tE_2}{\eta_1}}\right) + \frac{\sigma_0}{\eta}t \tag{3}$$

where σ_0 is the initial stress, E_1 and E_2 are constant moduli, η and η_1 are the long-term creep viscosities, t is the time when creep occurs and T_c is creep relaxation time representing the ratio of the viscosity coefficient (η_1) to Young's modulus (E_2).

2.2 Gas flow

2.2.1 Inorganic system

Flow within the inorganic systems is described by slip flow with a correction factor applied. Mass conservation for fluid flow in the inorganic systems is defined as (Zhang et al., 2008):

$$\frac{\partial m_{in}}{\partial t} + \nabla \cdot J_{in} = Q_c \tag{4}$$

where J_{in} is the mass flux of gas transport in the inorganic minerals and where Q_c is a coupling term to represent the mass exchange between organic and inorganic systems. This term accounts for the gas transitioning between adsorption/desorption in organic matter and free gas flow in the inorganic matrix. The coupling term integrates Langmuir-based adsorption/desorption dynamics into the model. This ensures accurate representation of mass transfer driven by pressure and concentration gradients.min represents the mass of gas in the inorganic system, which can be expressed as (Zhang et al., 2008):

$$m_{in} = \rho_{in}\phi_{in} \tag{5}$$

where ϕ_{in} is the porosity of the inorganic material and ρ_{in} is the gas density in the inorganic system. J_{in} is the mass flux, which is defined in terms of the pressure gradient as a modified Darcy equation:

$$J_{in} = -\frac{k_a}{\mu}\rho_{in}\nabla p_{in} \tag{6}$$

where μ is the dynamic viscosity of the gas and k_a is the apparent permeability of the inorganic system, which can be further expressed as (Cui et al., 2020a):

$$k_a = \left(1 + \frac{4Kn_{in}}{1+Kn_{in}}\right)k_{in\infty} \tag{7}$$

where $k_{in\infty}$ is the intrinsic permeability of the inorganic system and Kn_{in} is the Knudsen number in the inorganic system.

2.2.2 Organic system

The law of conservation of mass in an organic system is defined as(Zhang et al., 2008):

$$\frac{\partial m_{or}}{\partial t} + \nabla \cdot J_{or} = -Q_c \tag{8}$$

The gas mass content (m_{or}) is primarily adsorbed, which is defined as (Liu et al., 2010a):

$$m_{or} = \rho_{ga}\rho_{or}\frac{V_{Lor}p_{or}}{p_{or}+P_{Lor}} \tag{9}$$

where ρ_{ga} is the gas density under standard atmospheric pressure, ρ_{or} is the density of the organic matter, P_{Lor} is the Langmuir pressure constant in the organic system, and V_{Lor} is the Langmuir volume constant in the organic system.

The total mass flux (J_{or}) can be expressed in terms of effective diffusion and gas mass as:

$$J_{or} = -D_{ef}\nabla m_{or} \tag{10}$$

where D_{ef} is the effective diffusion coefficient of the organic matter system. Effective diffusion encompasses both gas with self-diffusion and Knudsen diffusion.

2.3 Permeability model

Shale contains four types of porosity: intergranular, intragranular, fractures, and organic pores. For modeling purposes, these have been consolidated into two primary categories: Inorganic and organic porosity. Inorganic porosity includes contributions from intergranular and intragranular pores, while organic porosity accounts for kerogen-related pores and fracture networks. The model equations focus on these two dominant porosity types, with the contributions of fractures and intra-grain pores integrated into the effective porosity for each matrix.

2.3.1 Intrinsic permeability-inorganic system

The porosity in the inorganic systems is related to the effective strain and can be defined as (Cui et al., 2018b):

$$\frac{\phi_{in}}{\phi_{in0}} = 1 + \frac{\alpha_{in}}{\phi_{in0}}\Delta\varepsilon_{ine} \tag{11}$$

where ϕ_{in0} is the initial porosity of the inorganic system, the subscript 0 is the initial value of the variable, and ε_{ine}
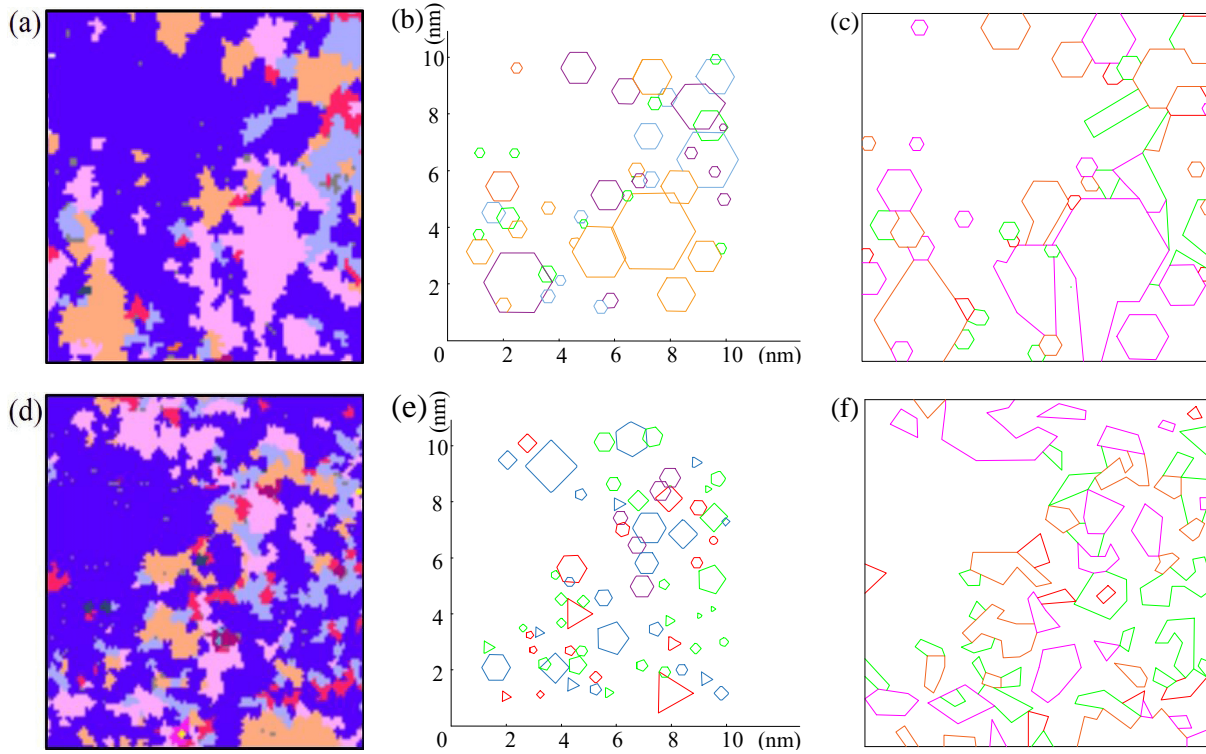
Fig. 1. Distribution of mineral phases: (a) Horizontal plane, (d) vertical plane; geometric depiction of the mineral phases in their initial state: (b) Horizontal plane, (e) vertical plane; geometric model depicts: (c) Horizontal plane, (f) vertical plane.

is the effective strain of the inorganic system, which can be expressed as (Liu et al., 2010a):

$$\Delta\varepsilon_{ine} = \Delta\varepsilon_{ing} + \Delta\varepsilon_{inl} \qquad (12)$$

The first term on the right represents the overall strain (ε_{ing}) of the shale, which mainly comprises the volumetric strain of the inorganic system and the strain caused by creep. The second term represents the local strain (ε_{inl}) of the inorganic system caused by gas pressure, which can be expressed as:

$$\Delta\varepsilon_{inl} = \frac{\Delta p_{in}}{K_{ins}} \qquad (13)$$

where K_{ins} is the bulk modulus of the inorganic skeleton.

A typical relationship between porosity and permeability is represented by the cubic law, which can be defined as (Liu et al., 2010b):

$$\frac{k_{in\infty}}{k_{in\infty 0}} = \left(\frac{\phi_{in}}{\phi_{in0}}\right)^3 = \left(1 + \frac{\alpha_{in}}{\phi_{in0}}\Delta\varepsilon_{ine}\right)^3 \qquad (14)$$

where $k_{in\infty}$ is the intrinsic permeability of the inorganic system, $k_{in\infty 0}$ is the initial intrinsic permeability of the inorganic system.

2.3.2 Effective diffusion-organic system

The effective diffusion coefficient (D_e) of an organic matter system is related to the effective strain as follows (Cui et al., 2020b):

$$\frac{D_e}{D_{e0}} = 1 + \frac{\alpha_{or}}{\phi_{or0}}\Delta\varepsilon_{ore} \qquad (15)$$

where D_{e0} is the initial effective diffusion coefficient of an organic matter system, ε_{ore} represents the effective strain of the organic matter system, which can be further expressed as:

$$\Delta\varepsilon_{ore} = \Delta\varepsilon_{org} + \Delta\varepsilon_{orl} \qquad (16)$$

The first term on the right side signifies the total strain (ε_{org}) of the organic matter system, mainly comprising the volumetric strain of organic matter and the strain induced by creep. The second term indicates the local strain (ε_{orl}) of the organic matter system, primarily consisting of the adsorption strain and compression strain of organic matter, which can be expressed as:

$$\Delta\varepsilon_{orl} = \frac{\Delta p_{or}}{K_{orm}} + \Delta\varepsilon_s(p_{or}) \qquad (17)$$

where K_{orm} represents the bulk modulus of organic matter. ε_s is the adsorption strain.

3. Model validation

3.1 System geometry

The shale matrix comprises two primary components: Inorganic minerals and organic matter. Maps of the distributions of mineral phases recovered from the TIMA automated mineral analysis system are utilized, as illustrated in Figs. 1(a) and 1(d) Based on the fractional percentages of different mineral components, a representative region is chosen where the volumetric proportion of each mineral component is equal to, or closely matches, that of the entire area. The fundamental

characteristics of this representative region are illustrated in Fig. 1, offering insights into the variations in gas production rates throughout the gas production process.

Avizo is employed to analyze the centroid, form factor, and equivalent diameter of different mineral clusters, thereby providing fundamentaldata for different mineral clusters. The following outlines the detailed methodology: Initially, the raw dataset (images) obtained via TIMA is imported into Avizo software for preprocessing, which includes noise reduction and segmentation. Segmentation tools in Avizo, such as thresholding and the watershed algorithm, are employed to distinguish mineral grains from the surrounding matrix. The segmented grains are then labeled for individual analysis. Subsequently, the spatial analysis module of Avizo is utilized to determine the centroid of each mineral grain. The centroid coordinates (x, y, z), representing the geometric center of the grains, are calculated based on voxel intensity and position. The shape factor, a dimensionless quantity reflecting the morphology of the grains, is computed for each mineral grain using the built-in modules. Similarly, the equivalent diameter of the grains is determined following the same procedure. Based on these data and on the equivalent tributary area principle, a simple geometric diagram is depicted using python code, as shown in Figs. 1(b) and 1(e).

Subsequently, a mineral phase distribution map is classified according to the algorithm, and the geometric model shown in Figs. 1(c) and 1(f) is described by the nearest neighbor method. Various boundary conditions indicate distinct shale components. In this representation, pink denotes calcite, orange signifies dolomite, green indicates clay, red represents pyrite, and the remaining portions correspond to quartz. Ultimately, the geometric model was imported into COMSOL Multiphysics (5.4) for further modeling.

3.2 Flow parameters

The gas flow and gas storage capacity of various minerals in the shale vary. Gas contents may be classified into two categories: Free gas and adsorbed gas. Free gas is predominantly stored within the pores of the inorganic minerals, such as calcite, dolomite, pyrite, and quartz. Adsorbed gas is primarily contained within the organic matter, primarily comprising clay minerals.

Shale typically contain four distinct types of pores: intragranular pores, intergranular pores, organic pores, and cracks (Gao et al., 2020). Intragranular pores are primarily located within the minerals of the shale, while intergranular pores are found between these minerals. Together, these two types of pores form the ensemble porosity. Variations in these pores result in differences in the gas storage state and content of these minerals. For a quantitative analysis of the porosity of each mineral component, (Wang et al., 2013) proposed a mathematical model based on the matrix porosity of the Longmaxi shale. The shale has three predominant types of pores: micropores in brittle minerals, organic micropores, and micropores between clay mineral layers. Consequently, this is represented this by a three-layer rock physics model, defining porosity as the sum of individual components in brittle, clay

and organic minerals as:

$$\phi = \rho A_b V_b + \rho A_c V_c + \rho A_t V_t \tag{18}$$

where ρ is the density of the shale, A is the mineral content, V is the pore volume per unit mass of each layer of rock, Subscripts b, c and t represent brittle, clay and organic matter, respectively. ϕ is the porosity of the shale and subscripts refer to brittle, clay and organic carbon components.

Building on this concept, an expression for porosity is refined for each mineral in the shale. The porosity of each component of the shale utilized in the cluster analysis can be expressed as:

$$\phi = \rho A_q V_q + \rho A_c V_c + \rho A_{ca} V_{ca} + \rho A_d V_d + \rho A_p V_p \tag{19}$$

where the subscripts q, c, ca, d, p represent quarter, clay, calcite, dolomite and pyrite, respectively. The porosity for each mineral can be determined by substituting these values into Eq. (19), as presented in Table 1.

Moreover, understanding the relationship between shale permeability and porosity is vital in representing gas flow in the subsurface environment. Previous studies have identified a log-linear relationship between shale porosity and permeability (Chen et al., 2015a; Qu et al., 2016; Shi et al., 2021), while others have refute this correlation (Chalmers et al., 2012; Zhang et al., 2014; Geng et al., 2016). A negative correlation between porosity and permeability in the Longmaxi shale has been observed (Yang et al., 2019) and is attributed to the impact of structure and texture on permeability. In conventional reservoir rocks, the pore throat diameter at 35% mercury saturation (r_p) in mercury injection tests is often utilized. The Winland equation, which describes the relationship among permeability (k), porosity (ϕ), and pore size (r_p), is given as (Aguilera, 2002):

$$r_p = 2.665 \left(\frac{k}{100\phi} \right)^{0.45} \tag{20}$$

When the pore sizes of various minerals in shale differ, then the permeability of various minerals in shale can be calculated from Eq. (20), as shown in Table 1.

The state of gas in shale minerals is assumed divided into free gas and adsorbed gas components. In this work, quartz, dolomite, calcite, and pyrite are classified as inorganic matter with organic matter mainly stored in clay minerals (Zhu et al., 2018). The proportions of gas content in different minerals are evaluated from Eqs. (5) and (9), as shown in Table 1.

3.3 Mechanical parameters

Nanoindentation was employed to characterize the mechanical properties at the individual mineral scale. The Longmaxi sample was prepared into a cubic sample 1 cm × 1 cm × 1 cm. The mechanical parameters of one hundred points were obtained in two different loading directions. The proportion of mineral components of the shale samples was obtained by XRD, and the proportion of each mineral component obtained. A Gaussian mixture model clustering analysis method was used to identify mineral clusters according to the distribution of mechanical parameters and the proportion of mineral com-

Table 1. Mineral properties and gas contents in shale.

Mineral	Density (kg/m^3)	Poisson's ratio	Porosity (%)	Permeability (1×10^{-17} m^2)	Gas content ratio (%)	Gas type
Calcite	2,710	0.28	2.37	0.979	7.51	Free
Dolomite	2,840	0.3	3.41	6.57	10.8	Free
Pyrite	5,000	0.32	01.35	0.557	4.28	Free
Quartz	2,650	0.2	1.8	39.8	5.71	Free
Clay	1,650	0.35	1.71	0.706	71.69	Adsorbed

Table 2. Micro-mechanical parameters of shale minerals.

Samples	Horizontal plane				Vertical plane			
	E_1 (GPa)	E_2 (GPa)	η (GPa·s)	η_1 (GPa·s)	E_1 (GPa)	E_2 (GPa)	η (GPa·s)	η_1 (GPa·s)
Calcite	57	0.28	19	250	66	59	22	310
Dolomite	43	23	34	7.8	48	27	4.2	9.2
Pyrite	66	54	9.6	140	83	73	11	200
Quartz	91	82	28	430	102	91	330	560
Clay	101	131	87	1,500	136	121	65	970

Table 3. Basic parameters for numerical modeling.

Parameters	Values	Parameters	Values
V_{Lor}	0.05	P_{Lor} (MPa)	5
μ (1×10^{-5} Pa·s)	1.84	ρ_{ga} (kg/m^3)	0.717
p_0 (MPa)	10	D_{ef} (1×10^{-12} m^2/s)	2.5

ponents. In this approach, the quantitative relationship between the micromechanical properties of the shale and mineral components was established. The micro-mechanical parameters obtained at mineral scale are displayed in.

In addition, some general parameters employed in the model are illustrated in Table 3.

3.4 Boundary conditions

This paper employs uniaxial strain and constant volume conditions as boundary conditions. The constant volume condition indicates that the overall volume of the representative elemental volume remains unchanged. In this scenario, the entire representative volume deforms neither horizontally or vertically, while the organic matter and inorganic minerals within the unit deform relative to each other. During gas production under uniaxial strain, the stress on the upper boundary remains constant. Thus, for the loading direction perpendicular to the bedding plane (horizontal plane), ta constant volume boundary condition is utilized. For the loading direction parallel to the bedding plane (vertical plane), invariant overburden pressure is applied.

The 'free triangle' feature in COMSOL Multiphysics (5.4) is utilized to mesh the geometric model, as illustrated in Fig.

2. Fig. 2(a) displays a full mesh with 10,928 domain elements and 1,152 edge elements, achieving a mesh unit quality of 0.85. Fig. 2(b) shows a mesh with 4,537 domain elements and 828 edge elements, with a mesh unit quality of 0.86. To facilitate the coupling process, the Darcy's law module and the solid mechanics module are selected to run together on the same mesh.

3.5 Model validation

The Gaussian decomposition method is utilized to fit the field gas production data. This method allows for the determination of the end time where gas production is exhausted (t_{end}) and the total gas volume recovered (Q_{total}) from the integral form of the Gaussian function. Additionally, the dimensionless time and dimensionless gas flow rate are employed for model verification. Dimensionless time enables the extrapolation of pore-scale simulation results to field-relevant timescales. While the simulation captures transient dynamics over short durations, the trends observed (e.g., rapid initial gas release and gradual stabilization) align with field-scale production profiles, validating the model's scalability and accuracy. The dimensionless time is defined as $t_\tau = t/t_{end}$, and the dimensionless gas flow rate is defined as $q_\tau = Q_t/Q_{total}$, where Q_t is the gas production within the time interval $2\Delta t$, defined as:

$$Q_t = \int_{t-\Delta t}^{t+\Delta t} q_\tau dt \tag{21}$$

To verify the model, the gas production process following hydraulic fracturing can be categorized into two distinct phases. Initially, gas migrates along the horizontal planes, followed by movement along the vertical plane. These combined
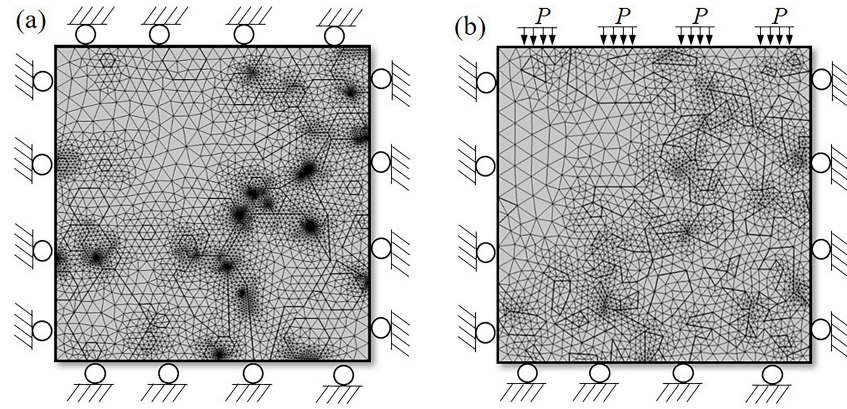
Fig. 2. Mesh geometry: (a) Horizontal plane and (b) vertical plane (Mesoscale).
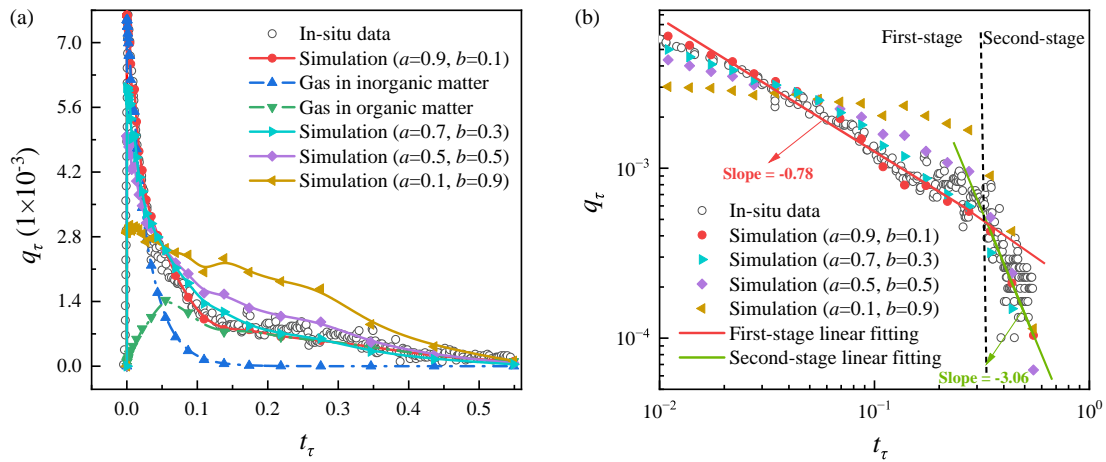
Fig. 3. Comparison of model results with field gas production data: (a) Contribution of different components to gas production and (b) two stages of gas production in log-log scale (Field scale).

transport directions represent the overall gas production process of shale gas. In relation to the simulation model, the gas production is depicted as the sum of the simulation outcomes of both planes (vertical and horizontal). By incorporating a contribution factor for each plane, the gas production process can be represented as:

$$Q_\tau = aQ_h + bQ_v \qquad (22)$$

where Q_τ represents the total gas production and Q_h and Q_v represent the gas production of the horizontal and the vertical planes, respectively. In this, a and b represent the fractional contributions of the horizontal plane and the vertical plane to the total gas production, respectively, where $a + b = 1$.

The model simulation results based on different contribution coefficients of two different planes are shown in Fig. 3. The figure shows that the model simulation data fit best only when the gas production in the horizontal plane accounts for a sufficiently large proportion. When $a = 0.9$ and $b = 0.1$, the best fit reaches 93.02%. This is primarily due to the cracks induced by shale hydraulic fracturing being predominantly oriented along the vertical plane, while the gas flow in the horizontal plane significantly contributes to the overall gas

production. Fig. 3(a) illustrates the contributions of various components to the gas production rate. As depicted, the gas in the inorganic minerals is initially discharged at a high flow rate, which then rapidly decreases. When the reduced extraction pressure reaches the organic matter, the adsorbed gas in the organic matter begins to desorb, serving as a supplementary supply. In the shale gas production process, the early stage primarily involves the recovery of free gas from inorganic minerals, whereas the later stage mainly involves adsorbed gas recovery from organic matter. Fig. 3(b) indicates that for a log-log scale, the shale gas production data reveal two stages with distinct slopes. The first stage is dominated by gas flow from the inorganic matter, while the second stage is mainly governed by gas flow from the organic matter.

4. Results

4.1 Permeability evolution in inorganic system

The evolution of permeability for each mineral within the inorganic system under varying boundary conditions during shale gas production is illustrated in Fig. 4. Under constant volume conditions, the trend of mineral permeability evolution
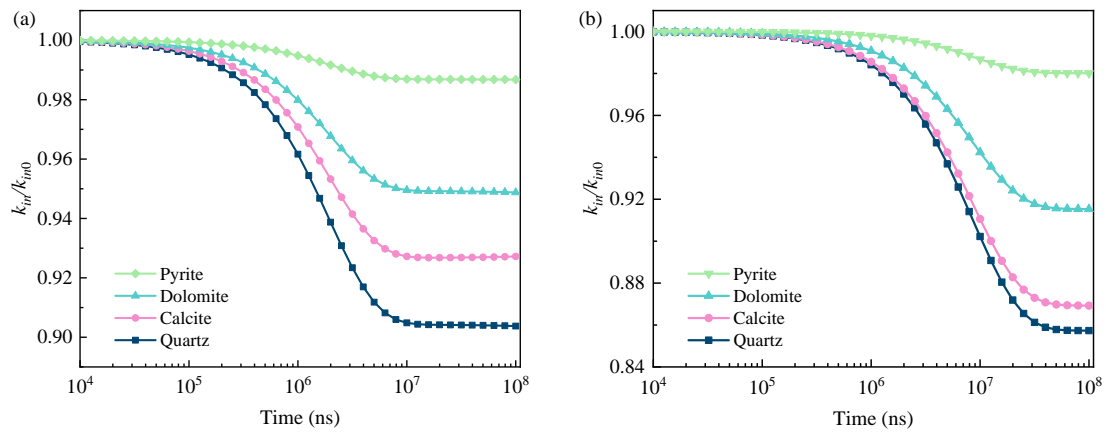
Fig. 4. Permeability evolution of each mineral component under different boundary conditions during shale gas production: (a) Constant volume and (b) uniaxial strain.
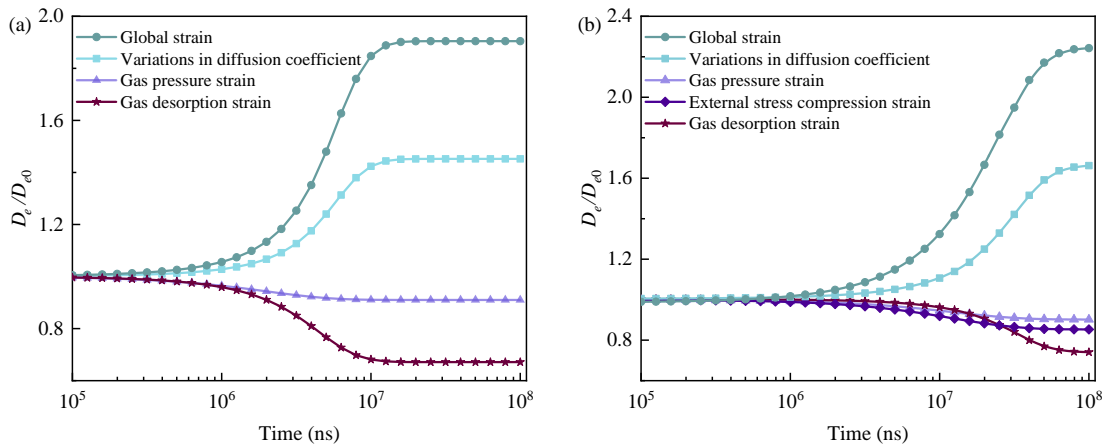
Fig. 5. Contributions of different mechanisms to the diffusion coefficient under different boundary conditions: (a) Constant volume and (b) uniaxial strain.

in the inorganic system remains consistent. The percentages of calcite, quartz, dolomite, and pyrite decline over time. This is primarily because, under constant volume conditions, minerals cannot freely expand outward, leading to a reduction in mineral permeability in the inorganic system as gas pressure decreases. Under uniaxial strain conditions, although the decreasing trend of mineral permeability in the inorganic system is similar, the extent of the decrease varies. This indicates that minerals with higher Young's moduli exhibit a smaller reduction in permeability during shale gas production and are relatively more stable. This is chiefly because the evolution of mineral permeability in the inorganic system is influenced by both global and local strains. Global strain results from the combined effect of volumetric strain and creep-induced strain of the inorganic minerals. Local strain is mainly caused by changes in gas pressure. Under these two boundary conditions, with the decline in gas pressure, local strain decreases while global strain also decreases, resulting in reduced mineral permeability in the inorganic system. Since the Young's modulus of quartz is lower than that of pyrite, the compressive strain of the organic matter will respond more significantly than quartz. Additionally, permeability under constant volume conditions

is greater than that under uniaxial strain conditions, primarily due to the control of fixed boundaries.

4.2 Evolution of effective diffusion coefficient in organic system

The evolution of the effective diffusion coefficient under constant volume and the contributions of various mechanisms are depicted in Fig. 5. The figure indicates that the evolution of the effective diffusion coefficient is primarily governed by three factors: The overall strain in the organic minerals, the organic gas pressure strain and the gas desorption strain. The gas pressure within the inorganic system exerts a confining pressure on the organic minerals. As the gas from the minerals in the inorganic system is extracted first, the gas pressure within these minerals decreases. Consequently, the organic minerals expand, leading to an overall strain that is manifest as an increase in the effective diffusion coefficient.

As gas production procedes in the organic system, the gas pressure decreases, leading to pore shrinkage and compression of the minerals in the organic system. This pore pressure strain results in a reduction in the effective diffusion coefficient.
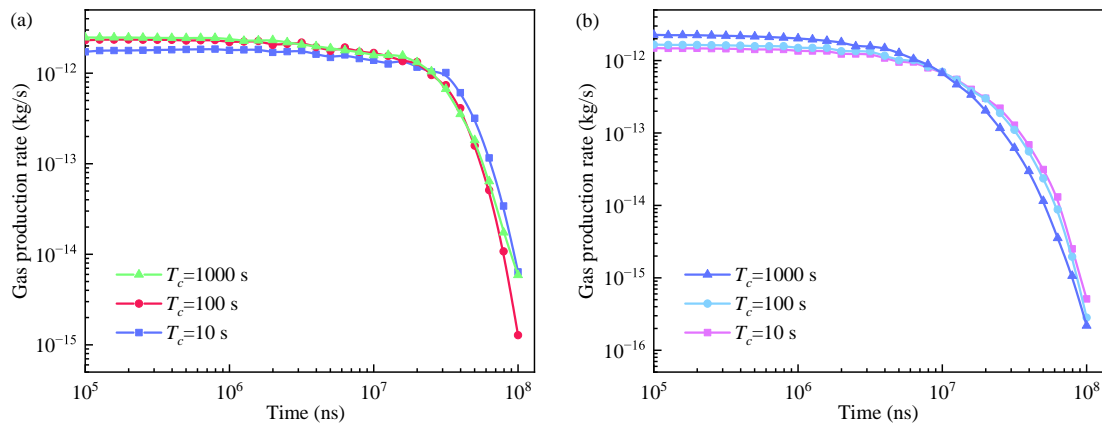
Fig. 6. Influence of creep relaxation time on shale gas production. Change in gas production rate on a log-log scale: (a) Horizontal plane and (b) vertical plane.

During this phase, as gas desorbs, the minerals in the organic system contract, and the adsorption strain further reduces the diffusion coefficient. This differs from the evolution of the effective diffusion coefficient under constant volume conditions. Under uniaxial strain conditions, the overall strain affects the effective diffusion coefficient in the organic system by introducing an external stress. This external stress compresses the overall strain, thereby decreasing the effective diffusion coefficient, as shown in Fig. 5(b).

4.3 Effects of creep behavior on gas depletion

Creep describes the gradual and continuous permanent deformation of a material subjected to constant stress over an extended period. During shale gas extraction, creep phenomena play a crucial role in affecting extraction efficiency and gas production rates, especially under conditions of high-pressure representative of deep extraction. Over time, the different mineral components within the shale show distinct creep behaviors on different planes. Initially, all creep curves rise quickly. The slopes of these curves then decrease, indicating a reduction in the creep rate, eventually reaching a more stable deformation rate corresponding to the steady-state creep phase.

The effects of creep on the horizontal and vertical planes are different. Quartz, calcite, and dolomite exhibit greater creep on the vertical plane compared to the horizontal plane, whereas pyrite shows greater creep on the horizontal plane than on the vertical plane. Notably, the creep effects of clay on both planes are essentially identical. This variation is related to the Young's moduli of the minerals and their individual shapes within the shale. The distribution of mineral particle sizes reveals that quartz particles are larger on the horizontal plane than on the vertical plane. Similarly, the particle sizes of calcite and dolomite are greater on the horizontal plane than on the vertical plane. For pyrite, the particle size is larger on the vertical plane than on the horizontal plane. The particle sizes of clay are consistent on both planes. This indicates that particle size is negatively correlated with creep; that is, larger particle sizes correspond to smaller creep values during gas production.

Moreover, the impact of creep relaxation time on shale gas extraction is examined on the two planes. The occurrence of creep reduces shale gas production. This reduction is primarily due to the closure of cracks and pore structures caused by creep, which prevents the release of some shale gas adsorbed on the rock surface, thereby decreasing the total recoverable gas volume. This phenomenon can directly affect the lifespan of shale gas extraction wells and the final recovery volume.

The shale gas production curve is also evaluated, with particular focus on the change in the shale gas production rate on a log-log scale, as depicted in Figs. 6(a) and 6(b). The figure illustrates that with increasing depletion time, the rapid decline in the gas production rate due to creep, becomes more pronounced. The closure of cracks and changes in rock pore structure caused by creep can accelerate the decline in the gas production rate. Additionally, the figure shows that the creep effect is not particularly significant in the early stages of production, but over time, its influence gradually intensifies, especially in the later stages. This intensification is mainly due to the cumulative effect of creep. Over time, the cumulative effects of creep on crack and pore structures lead to a long-term reduction in gas mobility, further affecting the production efficiency of shale gas wells. A comparative analysis of Fig. 6 indicates that the creep effect is directional, with different impacts on shale gas production in the horizontal and vertical planes.

4.4 Effect of Young's modulus of inorganic matrix on gas depletion

The effect of the inorganic Young's modulus on shale gas production is analyzed, as shown in Fig. 7. The figure shows that the gas production rate varies with the inorganic Young's modulus. The gas production rate changes differently with respect to the apparent Young's modulus on different planes. Figs. 7(a) and 7(b) show that with increasing quartz Young's modulus, the two-stage changes in the shale gas production rate also differ. Under a log-log scale, the main manifestation is that with increasing inorganic Young's modulus, the gas production curve in the first stage decreases less, whereas
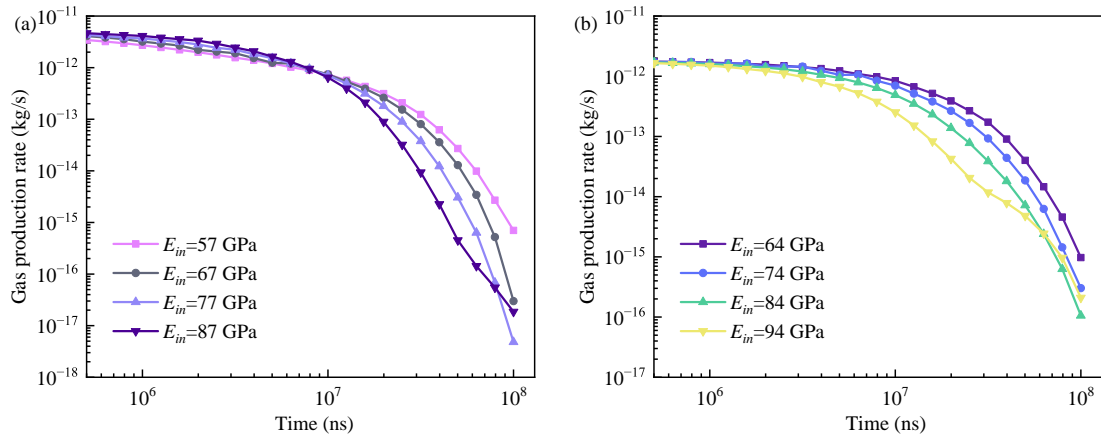
Fig. 7. Effect of Young's modulus of inorganic matter on shale gas production. Change in the gas production rate on a log-log scale: (a) Horizontal plane and (b) vertical plane.
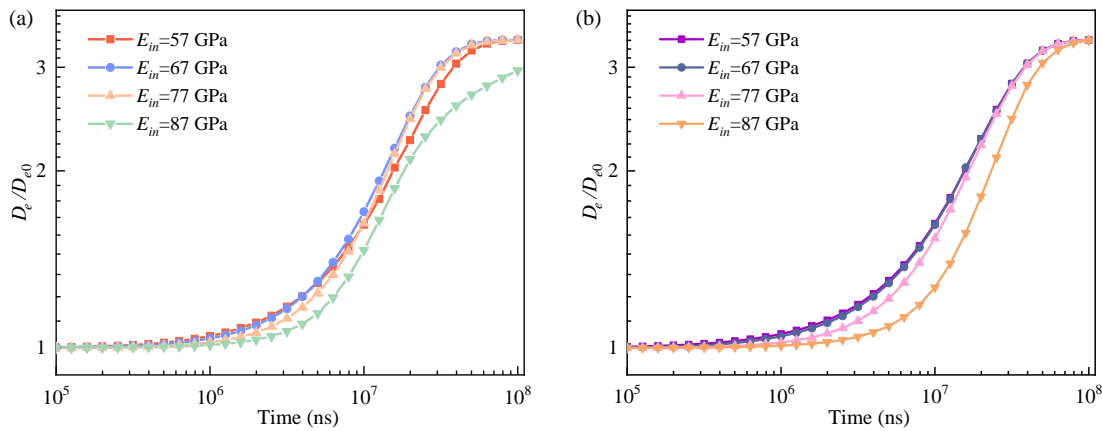
Fig. 8. Effects of different inorganic Young's moduli on the organic diffusion coefficient: (a) Horizontal plane and (b) vertical plane.

that in the second stage increases. Fig. 8 shows the effects of different inorganic Young's moduli on the diffusion coefficient of organic matter. Fig. 8 demonstrates that as Young's modulus of the inorganic matter increases, the diffusion coefficient decreases. This occurs primarily because an increase in Young's modulus of the inorganic matter reduces the overall contribution of strain to the diffusion coefficient of the organic matter. Consequently, this reduction leads to a decreased change in gas flow capacity in clay, resulting in a rapid decline in the gas production rate.

4.5 Effect of Young's modulus of organic matter on gas depletion

The impact of the organic Young's modulus on shale gas production is also analyzed, as presented in Fig. 9. The figure illustrates that the gas production rate exhibits different trends under varying organic Young's moduli. The changes in gas production rate with respect to Young's modulus differ across different orthogonal sections. Figs. 9(a) and 9(b) indicate that as the organic Young's modulus increases, the two-stage changes in the shale gas production rate also vary. In log-log

scale, it is evident that with an increasing organic Young's modulus, the gas production curve in the first stage decreases more significantly, whereas in the second stage, it decreases less.

Fig. 10 illustrates the influence of varying Young's moduli of organic matter on the organic matter diffusion coefficient. The figure shows that as Young's modulus of the organic matter increases, the diffusion coefficient of the organic matter also increases. This is primarily because the contribution of the overall strain to the organic matter diffusion coefficient grows with a higher Young's modulus. Concurrently, the negative correlation of the organic matter desorption strain and gas pressure strain on the diffusion coefficient weakens, leading to an increase in gas flow capacity and a slower decline in the gas production rate.

5. Discussion

5.1 Microstructural featurese

Mineral content has a significant impact on gas production history in shales. In complex shale mineral systems, the mechanical properties of different minerals and their
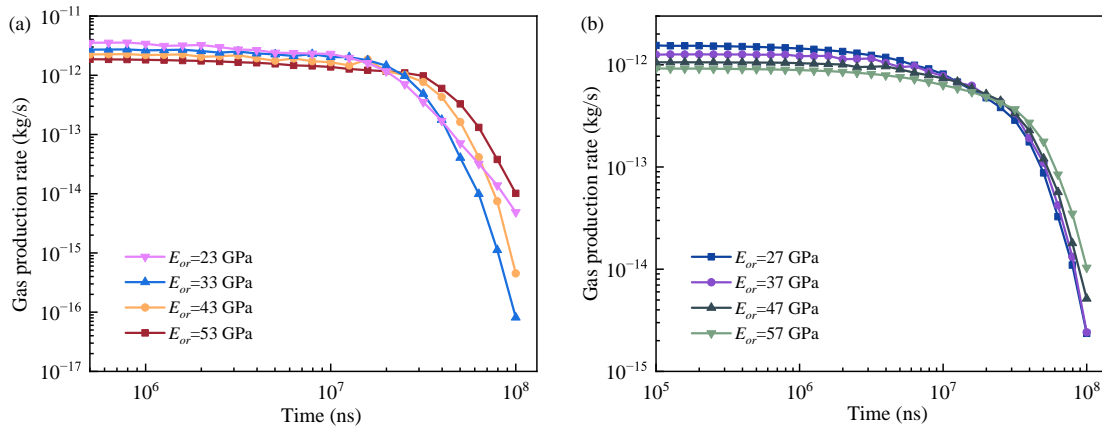
Fig. 9. Effect of Young's modulus of organic matter on shale gas production. Change in gas production rate on a log-log scale: (a) Horizontal plane and (b) vertical plane.
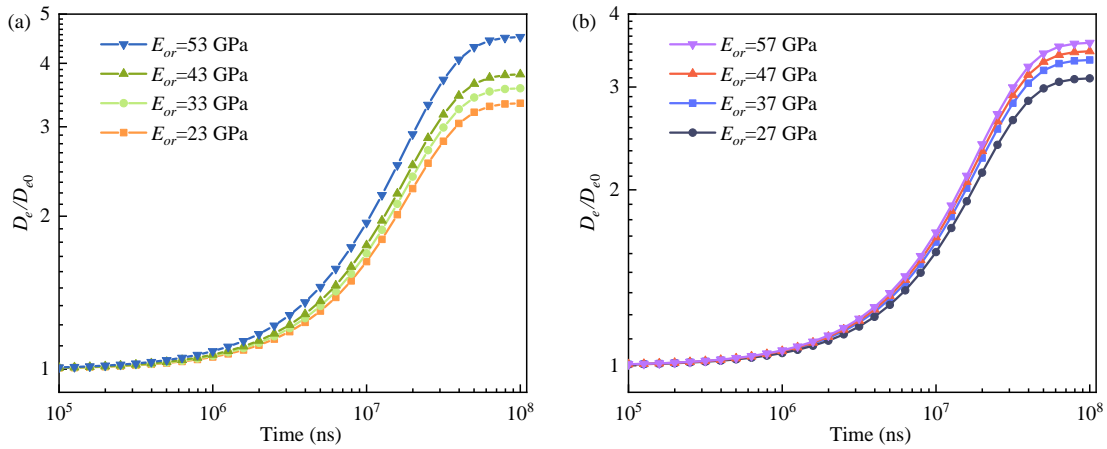

Fig. 10. Effects of different organic matter Young's moduli on the organic matter diffusion coefficient. (a) Horizontal plane and (b) vertical plane.

spatial distribution notably influence the overall mechanical behavior and permeability characteristics of the shale. For example, (Schwartz et al. (2019a)) observed that quartz-rich zones provide rigid frameworks, facilitating high permeability, while (Zhao et al. (2018)) highlighted how clay-rich regions hinder flow, creating permeability anisotropy. Such spatial heterogeneity directly impacts gas production efficiency and long-term reservoir performance. Inorganic minerals such as quartz and calcite typically exhibit high stiffness and strength, enabling them to effectively resist external stresses and maintain pore structure. However, these inorganic minerals often form discontinuous pore structures, leading to complex gas flow paths and potentially adverse effects on gas permeability. In contrast to inorganic minerals, organic matter (e.g., kerogen) possesses relatively lower stiffness and strength but demonstrates significant gas adsorption capacity. The Langmuir isotherm defines the maximum adsorption capacity and pressure dependency of gas desorption. As gas pressure declines during production, decreases, enabling desorbed gas to diffuse into the surrounding matrix. This mechanism is critical for stabilizing gas production during long-term extraction, as

observed in Fig. 11. Samples with high inorganic mineral content generally exhibit a high initial gas production rate, followed by a pronounced decline over time. This phenomenon is primarily attributed to the fact that gas within inorganic minerals exists predominantly in a free state, readily released during the initial stages of extraction. Conversely, samples with higher organic content tend to show lower initial gas production rates; however, as extraction continues, the adsorbed gas is gradually released, allowing for a constant rate of gas output over extended periods. In summary, shale with higher inorganic mineral content is more suitable for achieving high initial gas production, while shale with higher organic content demonstrates superior performance in maintaining sustained gas production over the long term. This distinction underscores the importance of considering both mineral composition and distribution in optimizing long-term gas recovery in shale reservoirs.

The size of mineral particles significantly influences the creep behavior of shale. As depicted in Table 2 and Fig. 6, larger particle sizes result in reduced creep effects. This reduction is due to the stronger interactions between larger m-
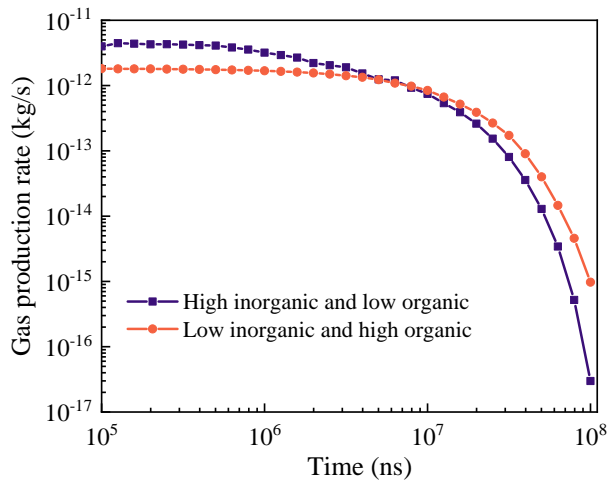
Fig. 11. Effect of mineral content on gas production. Gas production rate change on a log-log scale.
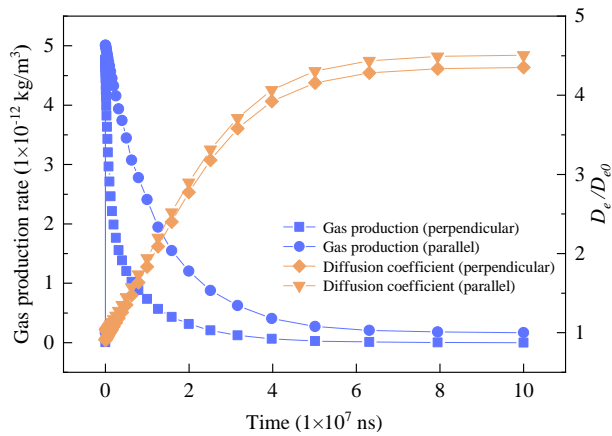
Fig. 12. Effect of shale anisotropy on gas production rate with time and diffusion coefficient.

ineral particles, which more effectively resist deformation and stress relaxation. Conversely, smaller mineral particles are more prone to deformation and creep because their interactions are relatively weaker. The simulation results presented in this study reveal that creep effects are notably pronounced under high-pressure conditions representative of deep environments. Minerals with larger particle sizes, such as quartz and calcite, generally exhibit lower creep characteristics, whereas minerals with smaller particle sizes, such as clay minerals, tend to show higher creep characteristics. This creep behavior not only affects the mechanical properties of shale but also directly impacts shale gas permeability and production. Consequently, optimizing the distribution of mineral particle sizes can significantly enhance the mechanical properties and extraction efficiency of shale gas reservoirs.

5.2 Mechanical properties

An analysis of the impact of the Young's modulus of both inorganic and organic matter on shale gas production demonstrates that mechanical properties exert a significant influence on the efficiency of gas production. The rate of gas production exhibits disparate trends when observed across different planes, contingent upon variations in the Young's modulus. Fig. 7 illustrates that as the Young's modulus of, inorganic quartz increases, the gas production rate of shale gas decreases significantly, in both stages, particularly when viewed in log-log space, where the gas production curve in the first stage shows a more pronounced decline. Furthermore, Fig. 8 illustrates the detrimental effect of the Young's modulus of the inorganic matter on the diffusion coefficient in the organic matter. This indicates that a high Young's modulus of the inorganic matter reduces the contribution of total strain to the diffusion coefficient, thereby impairing the flow capacity of gas in clay. This results in a rapid decrease in the gas production rate. In contrast, Figs. 9 and 10 demonstrate that although an increase in the Young's modulus of the organic matter results in a reduction in shale gas production rate, it has a positive impact on the diffusion coefficient of the organic matter. This is evident in the significant increase in the diffusion coefficient with the increase of Young's modulus. This mechanical behavior alters the inverse correlation between organic matter desorption strain and gas pressure strain, enhancing gas flow capacity and decelerating the decline in gas production rate. The Young's modulus of inorganic and organic matter exerts a differential influence on shale gas production. The elevated Young's modulus of the inorganic matter may reduce the efficiency of gas production, whereas the Young's modulus of the organic matter extends the duration of the gas production cycle. Consequently, the precise characterization of mechanical properties is of paramount importance for the prediction of shale gas production and the in optimizing development strategies.

The anisotropic nature of shale significantly influences its mechanical behavior and gas production efficiency. Due to the highly complex depositional and diagenetic environments, notable differences in mechanical properties and permeability are observed in the various directions. As illustrated in Fig. 12, when subjected to loading perpendicular to the bedding direction, shale typically shows a strong mechanical response while exhibiting low permeability. Conversely, when the load is applied parallel to the bedding direction, the mechanical response is comparatively weaker, but permeability is higher. This study demonstrates that Young's modulus and diffusion coefficients of shales vary considerably with different loading directions, directly impacting the shale gas production rate. Notably, the variance in diffusion coefficients between organic and inorganic materials in the different directions is particularly pronounced, further complicating the flow behavior of shale gas. Hence, during shale gas extraction, the anisotropic characteristics of shale must be considered and accommodated, with the selection of the appropriate extraction direction and method crucial to optimizing gas recovery rate.

5.3 Shortcomings and prospects

Although this study demonstrates the impact of micromechanical characteristics of shale gas reservoirs in affecting the gas production curve, this study is based on numerical modeling and lacks direct experimental validation of certain claims, particularly those related to spatial distribution effects.

Future work should integrate experimental observations to validate and refine the model's predictions. Meanwhile, full validation under controlled laboratory conditions, considering stress, temperature, and multiscale interactions, remains a necessary next step. Firstly, experimental conditions may introduce local deviations in research results. Experiments were conducted primarily in the laboratory. Despite efforts to simulate actual underground conditions, factors such as high pressure, high temperature and complex stress conditions could not be fully replicated. These actual underground conditions may significantly influence the mechanical properties and gas production behavior in shales. Also, laboratory conditions may not accurately reflect these influences, leading to discrepancies between experimental results and field conditions. Secondly, investigation of the influence of mineral interactions on the overall mechanical properties and permeability of shale remains limited. The complexity of combinations, interface properties and interaction mechanisms among different minerals is not fully understood. For instance, factors such as the contact mode between minerals, chemical bonding and microstructure interactions may significantly affect the mechanical properties of shale and its permeability. However, further exploration of these effects is necessary. Additionally, the distribution of various minerals in shale and their synergies may also impact shale gas output, yet current research in these areas remains insufficient.

Future research should concentrate on the following areas for comprehensive investigation. Firstly, interaction mechanisms between different minerals should be fully explored. Through detailed experimental observations and theoretical analysis, the microscopic interactions among minerals can be elucidated to enhance understanding of their effects on the mechanical properties and permeability of shale. Secondly, incorporating additional field data for model validation is necessary. Field data offer more realistic and comprehensive information. Comparing and validating experimental results with field data will facilitate the continuous optimization and enhancement of models and theories, thereby improving the reliability and applicability of research findings. Thirdly, advanced experimental techniques and numerical simulation methods should be employed. For instance, three-dimensional reconstructions can provide a more intuitive understanding of the internal structure of shale, while molecular dynamics simulations can model interactions at atomic and molecular levels. Utilizing these advanced technologies will grant deeper insights into the micromechanical behavior of shale.

6. Conclusions

A detailed analysis of the mechanical and transport properties of shale gas reservoirs at mineral scale is provided. Utilizing Burgers body model and poroelastic theory, the deformation behavior of the shale matrix during gas depletion is examined. A numerical model is constructed to simulate the interaction between heterogeneous mineral distributions and their impact on gas transport. The accuracy and practicality of such models are validated through comparison with field data. Additionally, the study elucidates key physical processes

in shale gas depletion, offering a theoretical foundation and technical guidance for the sustainable exploitation of shale gas reservoirs. The following conclusions can be drawn.

1) A shale microcreep-seepage coupling model is developed, which accounts for the complex physical processes and elucidates the intricate behavior of shale gas at the microscopic level. The study demonstrates that gas flow through the pores of inorganic minerals significantly contributes to gas production during the early stages of exploitation, while adsorbed gas in the organic matter becomes the primary contributor in the long-term production phase. Model verification, based on actual gas production data from Longmaxi formation shale gas wells, indicates high accuracy and practicality.

2) This study provides a detailed analysis of the variations in permeability of each mineral in the inorganic system and the effective diffusion coefficient of organic matter during gas erecovery. Additionally, it reveals the impact of different boundary conditions on these key parameters. Permeability decreases throughout the exploitation process, while changes in the diffusion coefficient are more complex, influenced by factors controlled by both global and local strain. Global strain increases the effective diffusion coefficient, whereas local strain-comprising gas pressure strain and desorption strain-decreases it.

3) The role of viscoelastic behavior of varied minerals in shale gas depletion behavior is systematically examined. The simulation results indicate that the creep effect is inversely proportional to mineral particle size: larger particles exhibit less creep. Additionally, the results reveal that creep significantly impacts the production and extraction efficiency of shale gas reservoirs, particularly under high-formation pressures representative of deep reservoirs. Creep-induced tightening of cracks and pore structures can obstruct gas release and reduce the cumulative recoverable gas volume.

4) The influence of mineral mechanical properties and gas flow characteristics on gas production is explored. Simulation results indicate that as Young's modulus of the inorganic matter increases, the decrease in the gas depletion curve during the first stage is less pronounced, while the curve in the second stage increases. Conversely, an increase in Young's modulus of the organic matter results in a greater decrease in the gas production history during the first stage and a smaller decrease in the second stage. Additionally, an increase in the Langmuir volume constant results in a greater reduction in the gas production rate during the first stage, while the reduction in the second stage decreases.

Conflict of interest

The authors declare no competing interest.

References

Abdallah, Y., Vandamme, M., Chateau, C., et al. Linking elastic properties of various carbonate rocks to their microstructure by coupling nanoindentation and SEM-EDS. International Journal of Rock Mechanics and Mining Sciences, 2023, 170: 105456.

Abedi, S., Slim, M., Ulm, F.-J. Nanomechanics of organic-rich shales: The role of thermal maturity and organic matter content on texture. Acta Geotechnica, 2016, 11(4): 775-787.

Aguilera, R. Incorporating capillary pressure, pore throat aperture radii, height above free-water table, and Winland r35 values on Pickett plots. AAPG Bulletin, 2002, 86(4): 605-624.

Al Ismail, M. I., Zoback, M. D. Effects of rock mineralogy and pore structure on stress-dependent permeability of shale samples. Philosophical Transactions of the Royal Society A, 2016, 374(2078): 20150428.

Ambrose, R. J., Hartman, R. C., Diaz-Campos, M., et al. New pore-scale considerations for shale gas in place calculations. Paper SPE 131772 Presented at the SPE Unconventional Gas Conference, Pittsburgh, Pennsylvania, USA, 23-25, February, 2010.

Chalmers, G. R., Ross, D. J., Bustin, R. M. Geological controls on matrix permeability of Devonian Gas Shales in the Horn River and Liard basins, northeastern British Columbia, Canada. International Journal of Coal Geology, 2012, 103: 120-131.

Chen, D., Pan, Z., Ye, Z. Dependence of gas shale fracture permeability on effective stress and reservoir pressure: Model match and insights. Fuel, 2015a, 139: 383-392.

Chen, F., Duan, Y., Wang, K., et al. A novel pressure transient response model considering multiple migration mechanisms in shale gas reservoir. Journal of Natural Gas Science and Engineering, 2015b, 22: 321-334.

Chen, T., Feng, X.-T., Cui, G., et al. Experimental study of permeability change of organic-rich gas shales under high effective stress. Journal of Natural Gas Science and Engineering, 2019, 64: 1-14.

Coq Germanicus, R., Mercier, D., Agrebi, F., et al. Quantitative mapping of high modulus materials at the nanoscale: Comparative study between atomic force microscopy and nanoindentation. Journal of Microscopy, 2020, 280(1): 51-62.

Cui, G., Liu, J., Wei, M., et al. Evolution of permeability during the process of shale gas extraction. Journal of Natural Gas Science and Engineering, 2018a, 49: 94-109.

Cui, G., Liu, J., Wei, M., et al. Why shale permeability changes under variable effective stresses: New insights. Fuel, 2018b, 213: 55-71.

Cui, G., Tan, Y., Chen, T., et al. Multidomain two-phase flow model to study the impacts of hydraulic fracturing on shale gas production. Energy & Fuels, 2020a, 34(4): 4273-4288.

Cui, G., Feng, X., Pan, Z., et al. Impact of shale matrix mechanical interactions on gas transport during production. Journal of Petroleum Science and Engineering, 2020b, 184: 106524.

Day-Stirrat, R. J., Dutton, S. P., Milliken, K. L., et al. Fabric anisotropy induced by primary depositional variations in the silt: Clay ratio in two fine-grained slope fan complexes: Texas Gulf Coast and northern North Sea. Sedimentary Geology, 2010, 226(1-4): 42-53.

Eliyahu, M., Emmanuel, S., Day-Stirrat, R. J., et al. Mechanical properties of organic matter in shales mapped at the nanometer scale. Marine and Petroleum Geology, 2015, 59: 294-304.

Feng, X., Yang, C., He, B., et al. Artificial intelligence technology in rock mechanics and rock engineering. Deep Resources Engineering, 2024, 1(2): 100008.

Gao, Z., Fan, Y., Xuan, Q., et al. A review of shale pore structure evolution characteristics with increasing thermal maturities. Advances in Geo-Energy Research, 2020, 4(3): 247-259.

Geng, L., Li, G., Zitha, P., et al. A diffusion–viscous flow model for simulating shale gas transport in nano-pores. Fuel, 2016, 181: 887-894.

Javadpour, F. Nanopores and apparent permeability of gas flow in mudrocks (shales and siltstone). Journal of Canadian Petroleum Technology, 2009, 48(8): 16-21.

Jin, Z., Li, W., Jin, C., et al. Anisotropic elastic, strength, and fracture properties of Marcellus shale. International Journal of Rock Mechanics and Mining Sciences, 2018, 109: 124-137.

Li, S., Dong, M., Li, Z. Measurement and revised interpretation of gas flow behavior in tight reservoir cores. Journal of Petroleum Science and Engineering, 2009, 65(1-2): 81-88.

Li, W., Wang, X., Cheng, J. Measurement of the anisotropic elastic properties of shale: uncertainty analysis and water effect. Bulletin of Engineering Geology and the Environment, 2019, 78: 6075-6087.

Liu, J., Chen, Z., Elsworth, D., et al. Evaluation of stress-controlled coal swelling processes. International Journal of Coal Geology, 2010a, 83(4): 446-455.

Liu, J., Chen, Z., Elsworth, D., et al. Linking gas-sorption induced changes in coal permeability to directional strains through a modulus reduction ratio. International Journal of Coal Geology, 2010b, 83(1): 21-30.

Liu, X., Chen, L., Sheng, J., et al. A Non-Equilibrium multiphysics model for coal seam gas extraction. Fuel, 2023a, 331: 125942.

Liu, Y., Burch, A. C., Bennett, K. C., et al. Bridging nanoindentation and triaxial creep tests on a shale. Acta Geotechnica, 2023b, 18(12): 6475-6487.

Loucks, R. G., Reed, R. M., Ruppel, S. C., et al. Morphology, genesis, and distribution of nanometer-scale pores in siliceous mudstones of the mississippian barnett shale.

Journal of Sedimentary Research, 2009, 79(12): 848-861.

Monteiro, P. J., Rycroft, C. H., Barenblatt, G. I. A mathematical model of fluid and gas flow in nanoporous media. Proceedings of the National Academy of Sciences of USA, 2012, 109(50): 20309-20313.

Oliver, W. C., Pharr G. M. An improved technique for determining hardness and elastic modulus using load and displacement sensing indentation experiments. Journal of Materials Research, 1992, 7(6): 1564-1583.

Palmer, I., Mansoori, J. How permeability depends on stress and pore pressure in coalbeds: A new model. SPE Reservoir Evaluation & Engineering, 1998, 1(6): 539-544.

Peng, Y., Liu, J., Pan, Z., et al. A sequential model of shale gas transport under the influence of fully coupled multiple processes. Journal of Natural Gas Science and Engineering, 2015, 27: 808-821.

Qu, H., Pan, Z., Peng, Y., et al. Controls on matrix permeability of shale samples from Longmaxi and Niutitang formations, China. Journal of Natural Gas Science and Engineering, 2016, 33: 599-610.

Schwartz, B., Elsworth, D., Marone, C. Relationships between mechanical and transport properties in Marcellus shale. International Journal of Rock Mechanics and Mining Sciences, 2019a, 119: 205-210.

Schwartz, B., Huffman, K., Thornton, D., et al. The effects of mineral distribution, pore geometry, and pore density on permeability evolution in gas shales. Fuel, 2019b, 257: 116005.

Shi, R., Liu, J., Wang, X., et al. A critical analysis of shale laboratory permeability evolution data. Energy, 2021, 236: 121405.

Tahmasebi, P., Javadpour, F., Enayati, S. F. Digital rock techniques to study shale permeability: A mini-review. Energy & Fuels, 2020, 34(12): 15672-15685.

Tian, H., Pan, L., Xiao, X., et al. A preliminary study on the pore characterization of Lower Silurian black shales in the Chuandong Thrust Fold Belt, southwestern China using low pressure N_2 adsorption and FE-SEM methods. Marine and Petroleum Geology, 2013, 48: 8-19.

Wang, L., Liu, B., Bai, L., et al. Pore evolution modeling in natural lacustrine shale influenced by mineral composition: Implications for shale oil exploration and CO_2 storage. Advances in Geo-Energy Research, 2024a, 13(3): 218-230.

Wang, S., Wu, Z., Chen, J., et al. Study of the effect of mineral components on the permeability impairment rate and stress sensitivity factor of shale. Geofluids, 2022, 2022(1): 4407252.

Wang, W., Chen, T., Cui, G., et al. New approach for predicting time-dependent deformation of shale rock: a modified fractional-order creep constitutive model. Bulletin of Engineering Geology and the Environment, 2024b, 83(6):

1-21.

Wang, Y., Dong, D., Yang, H., et al. Quantitative characterization of reservoir space in the Lower Silurian Longmaxi Shale, southern Sichuan, China. Science China Earth Sciences, 2013, 57: 313-322.

Xie, J., Xiong, W., Tan, Y., et al. Effects of Anisotropic Permeability Evolution on Shale Gas Production: An Internal Swelling Factor Model. Energy & Fuels, 2022, 36(2): 771-785.

Yang, C., Xiong, Y., Wang, J., et al. Mechanical characterization of shale matrix minerals using phase-positioned nanoindentation and nano-dynamic mechanical analysis. International Journal of Coal Geology, 2020, 229: 103571.

Yang, F., Ning, Z., Liu, H. Fractal characteristics of shales from a shale gas reservoir in the Sichuan Basin, China. Fuel, 2014, 115: 378-384.

Yang, F., Xu, S., Hao, F., et al. Petrophysical characteristics of shales with different lithofacies in Jiaoshiba area, Sichuan Basin, China: Implications for shale gas accumulation mechanism. Marine and Petroleum Geology, 2019, 109: 394-407.

Yang, R., Liu, X., Yu, R., et al. Long short-term memory suggests a model for predicting shale gas production. Applied Energy, 2022, 322: 119415.

Yuan, Y., Rezaee, R., Verrall, M., et al. Pore characterization and clay bound water assessment in shale with a combination of NMR and low-pressure nitrogen gas adsorption. International Journal of Coal Geology, 2018, 194: 11-21.

Zhang, H., Liu, J., Elsworth, D. How sorption-induced matrix deformation affects gas flow in coal seams: A new FE model. International Journal of Rock Mechanics and Mining Sciences, 2008, 45(8): 1226-1236.

Zhang, L., Li, D., Li, L., et al. Development of a new compositional model with multi-component sorption isotherm and slip flow in tight gas reservoirs. Journal of Natural Gas Science and Engineering, 2014, 21: 1061-1072.

Zhang, T., Li, X., Shi, J., et al. An apparent liquid permeability model of dual-wettability nanoporous media: A case study of shale. Chemical Engineering Science, 2018, 187: 280-291.

Zhang, W., Zhang, D., Zhao, J. Experimental investigation of water sensitivity effects on microscale mechanical behavior of shale. International Journal of Rock Mechanics and Mining Sciences, 2021, 145: 104837.

Zhao, P., Cai, J., Huang, Z., et al. Estimating permeability of shale-gas reservoirs from porosity and rock compositions. Geophysics, 2018, 83(5): MR283-MR294.

Zhu, X., Cai, J., Wang, G., et al. Role of organo-clay composites in hydrocarbon generation of shale. International Journal of Coal Geology, 2018, 192: 83-90.